

Rigidity of Epithelial Tissues as a Double Optimization Problem

Sadjad Arzash,^{1,2} Indrajit Tah,³ Andrea J. Liu,² M. Lisa Manning,¹

¹Department of Physics, Syracuse University, Syracuse, NY 13244, USA

²Department of Physics and Astronomy, University of Pennsylvania, Philadelphia, PA 19104, USA

³Speciality Glass Division, CSIR-Central Glass and Ceramic Research Institute, Kolkata 700032, India

How do cells tune emergent properties at the scale of tissues? One class of such emergent behaviors are rigidity transitions, in which a tissue changes from a solid-like to a fluid-like state or vice versa. Here, we introduce a new way that cells can tune rigidity using “adaptive degrees of freedom.” We study rigidity in vertex models, using the elastic energy as a cost function and the cell stiffnesses, target shapes, and target areas as sets of adaptive degrees of freedom that can be introduced to minimize the cost function. We show that the rigidity transition is unaffected when cell stiffnesses are treated as adaptive degrees of freedom. When preferred shapes or areas are treated as adaptive degrees of freedom, however, induced spatial correlations in target cell shapes or areas shift the rigidity transition. These observations suggest that tissues can tune properties at the cell-scale to obtain desired tissue-scale behaviors.

Introduction

Instructions for constructing biological tissues are encoded at the scale of molecules but drive collective tissue behavior at the multicellular scale. Similarly, in systems such as mechanical,

flow or electrical networks instructions encoded in the microscopic structure control collective properties. In materials design, the process of achieving a specific functionality typically involves a series of iterative steps in which the system is continually tested for desired functionality, adjusted based on feedback, and tested again to refine its performance. An effective strategy for solving this inverse problem of material design in these systems is gradient descent on a *cost function* that embodies the desired collective property by tuning microscopic *adaptive degrees of freedom* (DOFs), such as the presence or absence of a bond (1–4), bond stiffnesses (5, 6) or rest lengths in elastic networks, or conductances (5) in flow or electrical networks. Physics dictates that each system must also satisfy physical constraints during this process, imposed by minimizing the energy in elastic networks or dissipated power in flow or electrical networks, with respect to *physical degrees of freedom* (node positions in elastic networks, node pressures/voltages in flow/electrical networks).

Simultaneous minimization of the cost function and energy/power with respect to adaptive and physical degrees of freedom (*double optimization*) can be used to generate an auxetic (1, 3, 4) or allosteric response (2, 5). Alternatively, minimization of the energy/power while varying adaptive degrees of freedom according to local rules (7) can also be effective. Such local update rules include those that naturally occur in real materials, like directed aging (6, 8, 9), as well as rules that approximate gradient descent, as in Equilibrium Propagation (10) or Coupled Learning (11). These ideas have led to successful learning of desired properties in the lab (2, 6, 8, 12–14).

Here we show that biological tissues can potentially tune cell-scale properties, viewed as adaptive DOFs, to drive robust macroscopic, collective behaviors necessary for development and evolution. Our work focuses on rigidity transitions, which are a specific example of macroscopic collective behavior. Rigidity transitions occur when the tissue collectively switches back and forth from fluid-like behavior, where cells are able to rearrange neighbors and the tissue

can accommodate significant strain, to a solid-like behavior, where cells do not change neighbors and straining the tissue costs energy. Recent experiments demonstrates that tissues shift from a solid to a fluid (15, 16) or near-fluid state (17) as a function of space (15) and time (16), to facilitate flows necessary for body axis elongation (15–17) and organ formation (18, 19). A well-validated class of simple biophysical models (vertex (20–23), Voronoi (24), and cellular Potts (25) models) have successfully made quantitative predictions – with no fit parameters – for rigidity transitions in confluent epithelial tissues (16, 22, 26). A key feature of these models, which has been validated in experiments, is that the rigidity transition is controlled by cell shape, which is in turn tuned by expression and dynamics of biomolecules such as myosin and E-cadherin (27, 28).

In this paper, we explore the idea that developmental processes can usefully be regarded as double optimization processes, in which cell-scale adaptive DOF, such as cell shape, are adjusted to optimize a tissue-scale cost function that is minimized when the tissue achieves a desired macroscopic final state, while simultaneously staying in mechanical equilibrium. This viewpoint is bolstered by the recent finding that the *Drosophila* amnioserosa appears to shift its rigidity transition to remain rigid throughout the developmental process of dorsal closure by tuning preferred cell shapes continuously throughout the process (29). By framing a developmental process as a double optimization problem, we can unambiguously identify which cell-scale parameters are important for controlling a given macroscopic property. We argue that double optimization represents a theoretical framework for identifying cell-scale and molecular mechanisms that control larger-scale behavior, which is a major open problem in cell and developmental biology. This provides a systematic method for discovering what a tissue is optimizing during a given developmental process. In addition, this framework allows us to study an *ensemble* of tissue states that all minimize the same cost function. If we can identify common features in this ensemble that emerge from the double optimization process, we can then search

for such features in biological experiments.

This problem is also interesting from a physics perspective. Previous work has focused on over-constrained networks or jammed packings, in which the parameter that controls rigidity is the coordination number that describes the number of constraints per particle or node. This is because such systems become rigid when the number of degrees of freedom equals the number of constraints. Work by Hagh, et al. (30) introduced adaptive DOFs in the form of particle radii, and showed that these can be used to control rigidity over a wide range by tuning the coordination number, enabling the design of highly stable jammed states (30).

In contrast, vertex models are highly under-constrained, i.e., the number of physical degrees of freedom (vertex positions) is much larger than the number of constraints. Vertex models become rigid through geometric incompatibility, where cells are unable to achieve their target perimeters and areas. The system is stabilized due to energetic costs that occur only at second order in perturbations to the constraints (31), the same mechanism that drives strain-induced rigidity in sub-isostatic fiber networks (32–35). This raises the question of whether rigidity can be controlled in vertex models using adaptive DOFs.

As a first step towards addressing these open physics and biology questions, we investigate adaptive DOFs in 2D vertex models. We study how different sets of allowed adaptive DOFs – specifically, cell stiffnesses, preferred areas, or preferred perimeters – affect our ability to minimize a cost function. Here, as proof of principle, we make the simplest possible choice for the cost function, analogous to Ref. (30) for jammed packings : the total mechanical energy of the system. In other words, we explore the ability of different sets of adaptive DOFs to drive the system towards zero-energy floppy/fluidized states.

To characterize the sensitivity of vertex models to adaptive DOFs, we must also account for an important subtlety. Such models can be driven towards a fluid-like state by simply altering the mean (23) or the width (36) of the distribution of cell shapes. A similar result was discovered

in over-constrained jammed packings, where rigidity was found to be trivially dependent on the first and second moments of the radii distribution (30). As in that previous work (30), we avoid these trivial dependencies by fixing the distribution (or a set of its moments) and asking whether double optimization is able to introduce *spatial correlations* in the adaptive DOFs that are sufficient to shift the rigidity transition. If the system is able to learn, our next goal is to identify which adaptive DOFs are able to control the rigidity transition, and identify observable features that distinguish states that have learned from those that have not.

Results

Model

We study a 2D vertex model (21, 37), which describes a tissue monolayer as a network of polygonal cells. The physical DOF are the polygon vertices. Cellular properties and interactions are encoded in an energy function $E = \sum_i^N [K_{A,i}(A_i - A_{0,i})^2 + K_{P,i}(P_i - P_{0,i})^2]$, where A_i and $A_{0,i}$ are the actual and preferred areas, P_i and $P_{0,i}$ are the actual and preferred perimeters, $K_{A,i}$ and $K_{P,i}$ are the area and perimeter moduli of cell i . It is helpful to make the above equation dimensionless using $\langle K_{A,i} \rangle \langle A_{0,i} \rangle^2$ as the units of energy and $\sqrt{\langle A_{0,i} \rangle}$ as the units of length. We then have

$$e = \sum_i^N [k_{a,i}(a_i - a_{0,i})^2 + k_{p,i}(p_i - p_{0,i})^2], \quad (1)$$

where $\langle k_{a,i} \rangle = 1$, $\langle a_{0,i} \rangle = 1$, and p_i , $p_{0,i}$ are the dimensionless actual and preferred shape indices. Eq. 1 has been well studied for the case where $k_{a,i}$, $a_{0,i}$, $k_{p,i}$ have delta-function distributions, and $p_{0,i}$ has a distribution of zero (21, 23, 24) or nonzero width (36). Here, we study Eq. 1 using the open-source CellGPU code (38), promoting $k_{a,i}$, $a_{0,i}$, $k_{p,i}$ and $p_{0,i}$ to adaptive DOF. Initially, N cell centers are chosen from a uniform random distribution in a square box with length $L = \sqrt{N}$; vertices and edges are defined from a Voronoi tessellation of these points.

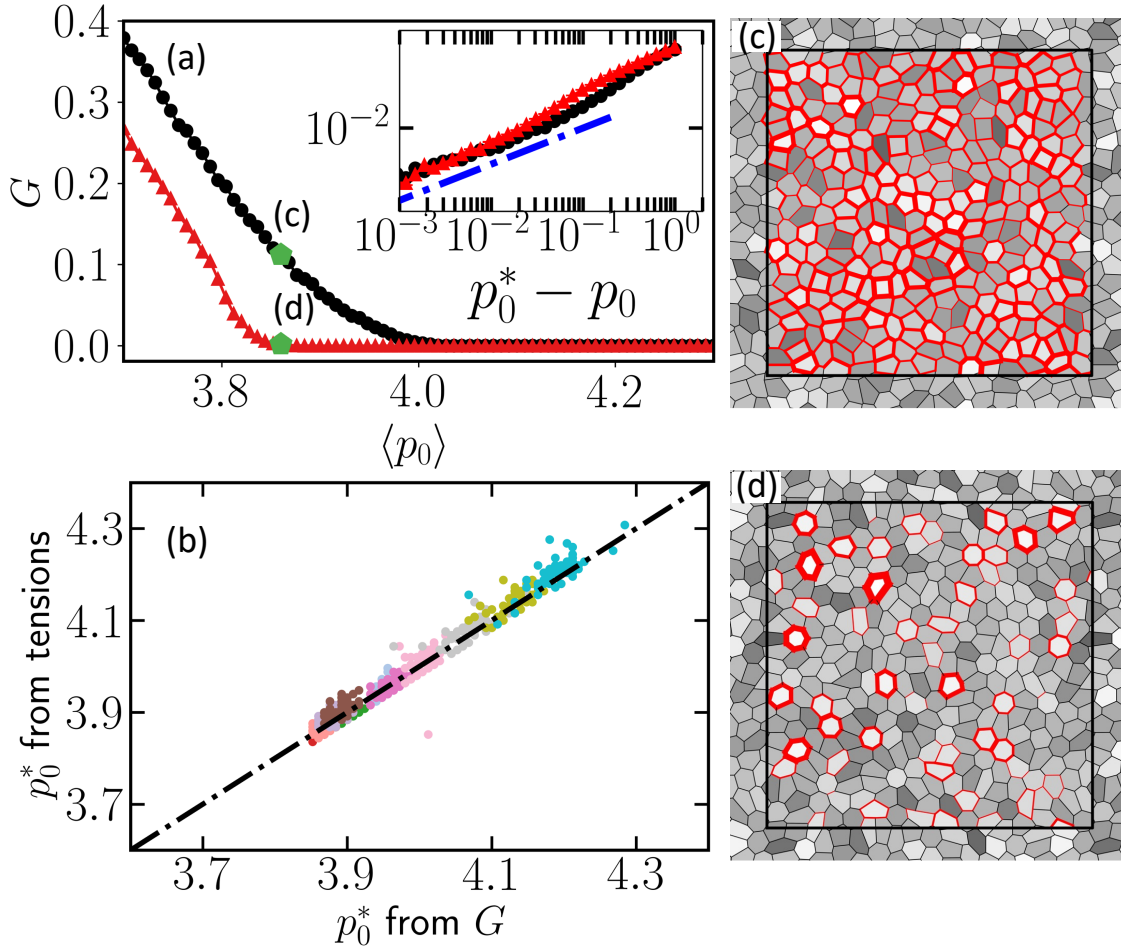


Figure 1: (a) Shear modulus G versus average target shape $\langle p_0 \rangle$ in vertex models with poly-disperse p_{0i} . Black curve (circles) shows minimization based solely on physical degrees of freedom, while red curve (triangles) includes both physical and $\{p_{0i}\}$ degrees of freedom. Inset illustrates shear modulus scaling; dashed blue line indicates a slope of 1.0. (b) Rigidity transition point p_0^* from edge tension percolation versus shear modulus G with different σ values for $\{p_{0,i}\}$ as degrees of freedom (DOF). Black dashed line represents $y = x$. (c, d) Tissue structures for highlighted points in (a). Cells are colored based on their $p_{0,i}$ values (higher $p_{0,i}$ is darker). Edge tensions are shown in red, with thickness proportional to tension. Both snapshots have the same distribution of target shape factors $\{p_{0,i}\}$.

The energy in Eq. 1 is minimized using the FIRE algorithm (39).

We investigate the impact of various sets of adaptive DOF separately; e.g., when $p_{0,i}$ are adaptive DOF, we initialize $p_{0,i}$ values from a Gaussian distribution with mean $\langle p_{0,i} \rangle$ and standard deviation σ , and set $k_{a,i} = k_{p,i} = a_{0,i} = 1$ for all cells. As in Hagh, et al. (30), we focus on the case where the cost function is simply the energy, or the physical cost function. Hagh et al. have shown that in sphere packings, minimizing the energy with respect to both physical DOF (particle positions) and adaptive DOF (particle radii) allows the system to find very rare low-energy states (30), shifting the jamming transition. We minimize the energy (Eq. 1) with respect to both physical DOF (vertex positions) and adaptive DOF to study the influence of adaptive DOF on the rigidity transition. We keep the adaptive DOF distributions approximately fixed by imposing constraints on sets of moments of the distribution, such as the $m = \{-1, -2, -3, 1, 2, 3\}$ moments (see the SI). This constrained minimization method ensures the distribution of adaptive DOF stays fixed during our minimization dynamics. We also perform zero-temperature swap minimization to fix the distribution exactly. In this method, each of the N cells maintains its preferred property (introducing N constraints), cells are swapped in a trial move, and moves that lower the energy are accepted (see SI).

We evaluate rigidity based on the shear modulus G (40): $G > 0$ in the rigid phase, and $G = 0$ in the fluid phase. To compute G , we freeze all adaptive DOF (see SI). Unless otherwise stated, error bars show the standard deviation over 50 samples.

Introducing target shapes and areas as adaptive degrees of freedom can fluidize tissues

As the preferred shape index p_0 increases, confluent tissues with only physical degrees of freedom experience a solid-fluid phase transition at a critical value p_0^* (23, 34). For systems with polydisperse $p_{0,i}$, the critical point p_0^* shifts towards larger average preferred shape factors with

increasing standard deviation σ of the p_0 distribution (36) (black data in Fig. 3a). For a system with $p_{0,i}$ drawn from a Gaussian distribution with $\sigma = 0.2$ (16), we find $p_0^* = 4.05 \pm 0.02$ (curve with black circles in Fig. 1a). As $p_0 \rightarrow p_0^{*-}$, approaching the transition from the rigid side, the shear modulus vanishes as a power law: $G \approx a(p_0^* - p_0)^b$ with $b = 1.0$ (23, 34). We subtract a finite-size-effect offset (see SI) and fit to this form to see how the scaling exponent b and the position of the rigidity transition, p_0^* , change as we introduce different sets of adaptive DOF.

Rigidity is associated with percolation of edges (cell-cell junctions) with nonzero tensions (36). The tension of edge ij separating cells i and j is $T_{ij} = 2K_{P,i}(P_i - P_{0,i}) + 2K_{P,j}(P_j - P_{0,j})$, which when nondimensionalized becomes:

$$t_{ij} = 2k_{p,i}\sqrt{a_{0,i}}\tau_i^p + 2k_{p,j}\sqrt{a_{0,j}}\tau_j^p, \quad (2)$$

where $\tau_i^p = p_i - p_{0,i}$ is the tension of cell i in units of $\langle K_{A,i} \rangle \langle A_{0,i} \rangle^{3/2}$, i.e., energy/length. For $p_0 < p_0^*$, a percolating cluster of nonzero edge tensions (Fig. 1) maintains mechanical rigidity of tissue (36). For $p_0 > p_0^*$, nonzero edge tensions fail to percolate and the tissue is fluid – it cannot resist shear deformation.

We first note that p_0^* is unaffected when the cell perimeter stiffnesses $\{k_{p,i}\}$ in Eq. 1 are allowed as adaptive DOF (Fig. 2). Clearly, manipulating $k_{p,i}$ cannot affect percolation of nonzero edge tensions if all the $k_{p,i}$ are positive. Therefore, allowing $k_{p,i}$ as adaptive DOF does not affect the rigidity transition. The scaling exponent b also remains unchanged but the tissue softens (see SI).

We next consider variations in cell area stiffnesses $k_{a,i}$ as adaptive DOF with $a_{0,i} = 1$, $k_{p,i} = 1$ and $p_{0,i} = p_0$ for every cell i . One might expect the system to distribute its cell areas a_i to be closer to $a_{0,i} = 1$ for cells with larger values of $k_{a,i}$, leading to correlations that shift the transition. However, vertex models are unstressed at the rigidity transition (31), so their properties there cannot depend on $k_{a,i}$. As a result, the rigidity transition is unaffected by

introducing $k_{a,i}$ as adaptive DOF.

We now consider preferred shape indices $\{p_{0,i}\}$ as adaptive DOF. Upon minimization, tissues adjust the values of some individual preferred shape indices $p_{0,i}$ to lower the energy by eliminating $p_i - p_{0,i}$. This leads to a lower fraction of nonzero tension edges, shifting the rigidity transition p_0^* to lower values (red triangles in Fig. 1a). Thus, minimizing E with respect to $p_{0,i}$ as well as the vertex positions introduces spatial correlations in $p_{0,i}$ that fluidize a tissue that would otherwise be solid. This shift persists whether we constrain certain moments of the p_0 -distribution or preserve the distribution exactly (see Fig. 2). The scaling exponent b for the shear modulus remains unaffected within our error bars (see SI). Moreover, the amplitude a of the shear modulus decreases more than when $k_{p,i}$ or $k_{a,i}$ are adaptive DOF (see SI).

Since allowing shape indices as degrees of freedom shifts p_0^* , we expect that it also alters the vibrational density of states that describes the curvatures of the potential energy landscape in the rigid phase near p_0^* . As shown in the SI, double optimization on the $\{p_{0,i}\}$ DOFs reduces the curvatures and shifts the normal modes to lower frequencies. While previous work has suggested that additional signatures of double optimization, such as high-curvature directions in the cost function (41, 42), can be found in eigenmodes of the cost Hessian, which in this case are identical to the vibrational normal modes since the cost function is simply the energy, we do not find any such signatures here. We conjecture that this is because the cost landscape and physical landscapes are already identical from the beginning of the double optimization process. As a result, there is no way in which double optimization can leave imprints on the energy landscape through coupling of two distinct landscapes.

Allowing $p_{0,i}$ as adaptive DOF not only shifts p_0^* but also increases the amount of structural order in the tissue (see SI). This ordering feature can be seen by sharper peaks in the pair correlation function. Consistent with this observation, we find a higher fraction of hexagonal cells f_6 when $\{p_{0,i}\}$ are added as new DOF (see SI). Importantly, the range of f_6 , from 0.3 to 0.65, is

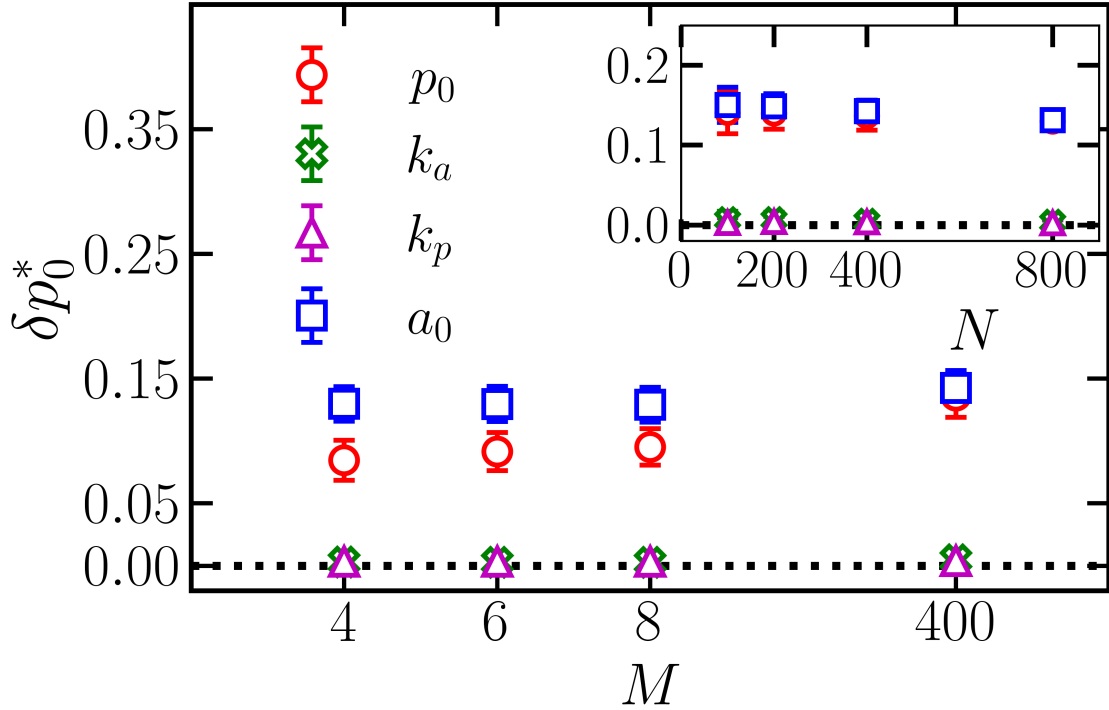


Figure 2: Change in the rigidity transition point δp_0^* after introducing different transient degrees of freedom (different symbols), as a function of the number of constraints M on the distribution. Inset shows how δp_0^* varies with N for $M = 400$. The zero-temperature swap system is indicated by 400 constraints, the number of cells in the tissue. These results correspond to a standard deviation of $\sigma = 0.2$ of transient DOF.

tunable through adjustments in the mean and standard deviation of the $\{p_{0,i}\}$ distribution. This property can be used to mimic the level of hexagonal cells in epithelial tissues, which has been shown to change substantially between different stages of development (43).

Non-monotonic relationship between rigidity shift and distribution width

So far, we have used a fixed standard deviation ($\sigma = 0.2$) for the distribution of $\{p_{0,i}\}$. However, σ significantly influences tissue rigidity (36), shifting p_0^* upwards (36) (black circles in Fig. 3a). This raises the question: how does the shift in the transition p_0^* due to adding $p_{0,i}$ as adaptive DOF vary with σ ? We observe a reduction in p_0^* at all σ (compare the red triangles to black circles in Fig. 3a). Interestingly, the magnitude of this reduction is non-monotonic. The purple curve in Fig. 3a, δp_0^* , shows that the shift in the transition is maximal at $\sigma \approx 0.15$. This suggests there is an optimal level of cell-to-cell fluctuations in biological tissues that enables double optimization to modulate rigidity.

To understand this non-monotonicity, we first note that as σ approaches zero, the $\{p_{0,i}\}$ distribution approaches a delta-function and there are no adaptive DOF. Therefore, δp_0^* must increase away from that point. To understand why δp_0^* decreases for $\sigma \gtrsim 0.15$, we analyzed the correlations between p and p_0 across all cells, both with and without p_0 as adaptive DOF. As expected, the Pearson's correlation coefficient $\rho(p, p_0)$ rises when we incorporate cell p_0 values as adaptive DOF across all σ values (see SI); the energy is lowered by bringing p_i closer to $p_{0,i}$. But for $\sigma \gtrsim 0.15$, p and p_0 already exhibit strong correlations even when $p_{0,i}$ are not adaptive DOF. Introducing $p_{0,i}$ as adaptive DOF only marginally enhances this correlation, so δp_0^* decreases as shown in Fig. 3.

Finally, we consider the preferred cell areas, $A_{0,i}$. In tissues where $A_{0,i} = A_0$ is the same for all cells, altering A_0 while keeping P_0 fixed does not affect p_0^* due to the confluency constraint ($\sum A_i = \text{constant} = L^2$) (44, 45). Yang et al. (44) found that the difference between A_0 and

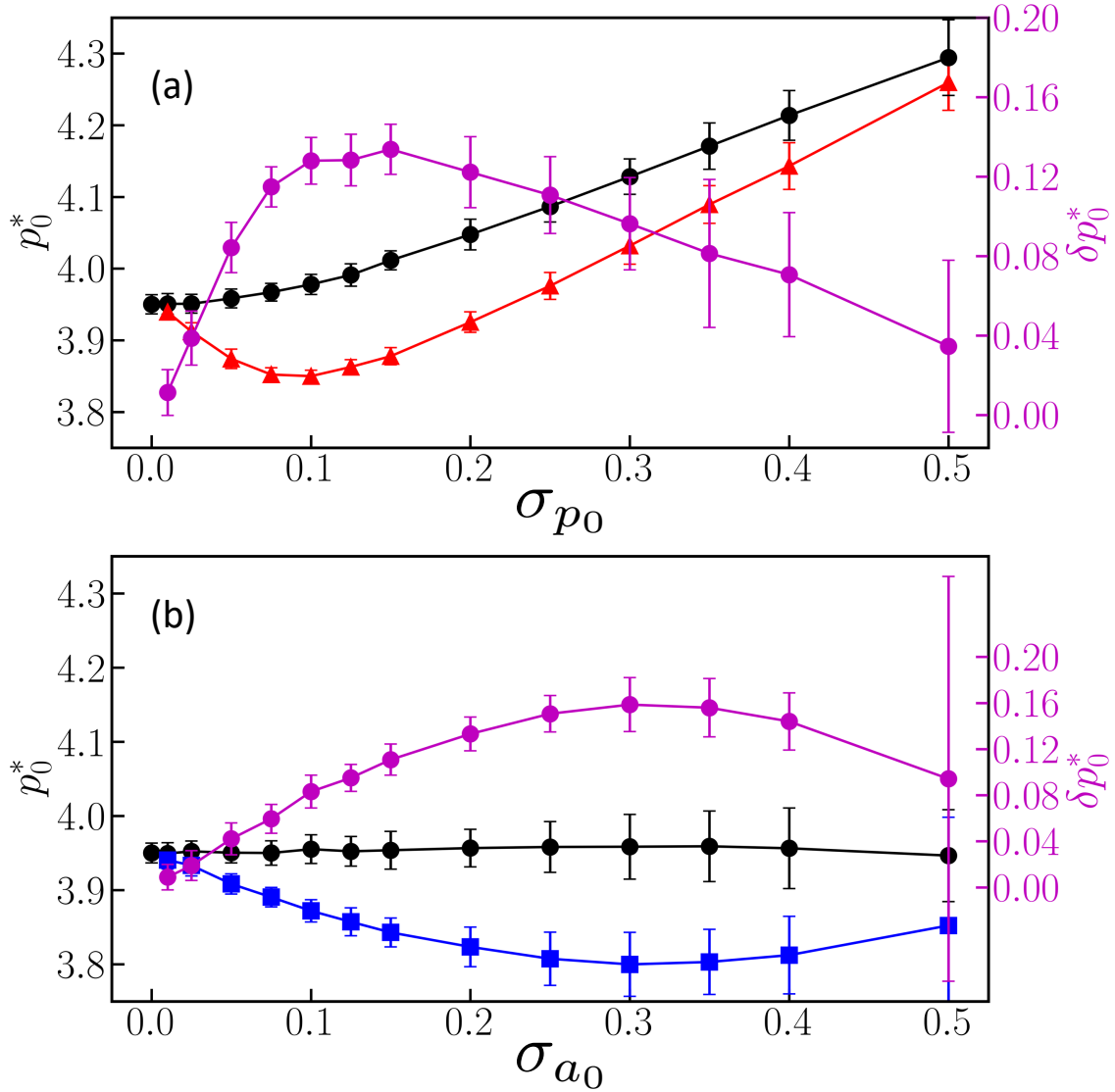


Figure 3: The effect of polydispersity of adaptive DOF distributions on the rigidity transition point. (a) The left axis shows the transition point p_0^* versus the standard deviation σ_{p_0} of the $\{p_{0,i}\}$ distribution. When only vertex positions can vary during energy minimization (black circles), p_0^* increases with σ_{p_0} . However, when $\{p_{0,i}\}$ are also allowed to vary (red triangles), the behavior of p_0^* versus σ_{p_0} becomes non-monotonic. The right axis δp_0^* shows the reduction of p_0^* due to adding $\{p_{0,i}\}$ as degrees of freedom. (b) Same as (a), but with $\{a_{0,i}\}$ allowed to vary instead of $\{p_{0,i}\}$.

the actual area $\langle A \rangle = N/L^2$ alters the overall pressure of the system, but not the shear stresses. We find that even in the presence of heterogeneous $A_{0,i}$ values, p_0^* is unaffected by changes in the *average* target area $\langle A_0 \rangle$ (see SI), so in what follows we hold $\langle A_0 \rangle = 1$ fixed. The solid black circles in Fig. 3b shows that varying the *width* of the distribution of the dimensionless $a_{0,i}$ in Eq. 1 also does not affect the transition point. Note that defining target shape factors as $P_{0,i}/\langle A_i \rangle$ would introduce variability in the transition point with σ_{a_0} (see SI). This suggests that the enhanced rigidity discussed in Ref. (36) is caused by heterogeneity in target shape indices ($p_{0,i} = P_{0,i}/\sqrt{A_{0,i}}$) and not by heterogeneity in $P_{0,i}$.

Given these results, we promote $\{A_{0,i}\}$ to adaptive DOF while keeping $\langle A_{0,i} \rangle$ fixed. This introduces *two* sets of adaptive DOF in the dimensionless energy in Eq. 1, namely $\{a_{0,i}\}$ and $\{p_{0,i}\}$. We have already shown how introducing $\{p_{0,i}\}$ as adaptive DOF affects rigidity, so now we consider the effects of $a_{0,i}$ in isolation. To do so, we maintain a constant target shape factor for cells, i.e., $p_{0,i} = p_0$, by coupling the target perimeters $\{P_{0,i}\}$ with the target areas: $\{P_{0,i} = p_0\sqrt{A_{0,i}}\}$. This allows us to consider only $\{a_{0,i}\}$ while keeping the average $\langle A_{0,i} \rangle = 1.0$ at homogeneous $p_{0,i} = p_0$. We find that introducing $\{a_{0,i}\}$ as adaptive DOF leaves the scaling exponent for the shear modulus unchanged (see SI). Similar to $\{p_{0,i}\}$, the $\{a_{0,i}\}$ adaptive DOF shift the transition downwards. This occurs at all values of the width of $\{a_{0,i}\}$ distribution, σ_{a_0} , with the maximum shift occurring around $\sigma_{a_0} \approx 0.3$. Correlations in $a_{0,i}$ from cell to cell causes τ_{ij} in Eq. 2 to vanish for some edges, shifting the percolation of nonzero tensions to lower p_0^* .

Discussion

We have explored the effects of adding adaptive degrees of freedom in 2D vertex models on the rigidity transition point, p_0^* . The transition is unaffected when cell stiffnesses K_A and K_P are allowed to vary. In contrast, introducing preferred cell areas or perimeters as adaptive degrees of freedom significantly alters the tissue's energy landscape, shifting p_0^* downwards.

Learned spatial correlations in p_0 or a_0 can fluidize a tissue, and there are optimal values for the heterogeneity in p_0 ($\sigma_{p_0} \approx 0.15$) and a_0 ($\sigma_{a_0} \approx 0.3$) that lead to the largest shift of the transition.

adaptive DOF have previously been introduced into networks that become rigid when the number of physical degrees of freedom equals the number of physical constraints (1, 3, 4, 30). In contrast, vertex models are highly under-constrained, and become rigid through geometric incompatibility (31). Our finding that rigidity in these models is also strongly affected by adaptive DOF suggests that vertex models can be used to study epithelial mechanics in terms of double optimization processes.

It is well-established that systems with fixed topology can learn intricate tasks (7). While Hagh et al. (30) demonstrated that jammed particle packings subject to frequent rearrangements can learn to identify ultra stable states, it is difficult to tune arbitrary mechanical responses into *typical* jammed states because they are marginally stable to rearrangements (46). Confluent epithelial tissues lie in an intermediate state between these two extremes – topological rearrangements, primarily in the form of T1 transitions, can occur but are not nearly as prevalent as in jammed packings. Our finding that preferred shape indices and cell areas effectively tune rigidity in vertex models suggests that introducing them as adaptive DOF could be a fruitful way of obtaining complex responses in systems that allow topological rearrangements.

The framework of physical learning with $\{p_{0,i}\}$ or $\{a_{0,i}\}$ as adaptive DOF could provide a new paradigm for understanding biological tissue mechanics. Individual cells can control cell- and molecular-scale properties, including the concentration of adhesion molecules and myosin motors, which in turn govern the preferred shape index locally (16, 27). Our work indicates that tissues should be able to learn if they follow a global gradient closely enough. In other systems, it has been possible to identify local learning rules that project sufficiently onto the global gradient to allow double optimization (6, 8, 9, 11, 12). It would be interesting to study whether local rules governing the dynamics of cell shapes and tensions that have already been

proposed (17, 47, 48) project onto gradients of useful global cost functions, or conversely, to hypothesize cost functions for tissues and search for possible local learning rules that enable them to be minimized. More broadly, this framework could be useful for predicting how the dynamics of tissues arises from variation of cellular properties across developmental or evolutionary timescales.

Materials and Methods

Details of energy minimization

To simulate a 2D vertex model, we use the CellGPU open-source code (38). We randomly generate cell positions in a periodic square box of lateral length $L = \sqrt{N}$, where N is the number of cells. We create the initial tissue by Voronoi tessellation of these points. In order to analyze the mechanical behavior of biological tissues at zero temperature, we minimize the elastic energy in Eq. (1) using FIRE (39). Once we achieve the minimum energy state, we calculate properties such as linear shear modulus G to determine the mechanical stability of our system. Below, we briefly explain how to compute forces in a vertex model as well as how to perform energy minimization with various degrees of freedom.

Minimizing energy with respect to physical degrees of freedom

The individual cell areas and perimeters are calculated from positions of vertices $\{\vec{r}_m\}$ associated with that cell. For a cell i with n vertices (or number of neighbors), we have

$$\begin{aligned}
 P_i &= \sum_{m=1}^n \|\vec{r}_{m+1} - \vec{r}_m\| \\
 A_i &= \frac{1}{2} \sum_{m=1}^n (\vec{r}_{m+1,x} + \vec{r}_{m,x})(\vec{r}_{m+1,y} - \vec{r}_{m,y})
 \end{aligned}
 \tag{3}$$

where the summation goes counterclockwise around vertices of the cell and we define $\vec{r}_{n+1} = \vec{r}_1$. For finding the area of a polygon, we use the trapezoid formula. However, other formulas

like the shoelace or triangle formulas can also be used. The total force on vertex m is computed by adding the force contribution of its three adjacent cells. The α component of the force contribution of cell i on vertex m is

$$f_{m,\alpha}^i = -\frac{\partial e_i}{\partial r_{m,\alpha}} = -2k_{a,i}(a_i - a_{0,i})\frac{\partial a_i}{\partial r_{m,\alpha}} - 2k_{p,i}(p_i - p_{0,i})\frac{\partial p_i}{\partial r_{m,\alpha}}, \quad (4)$$

where the derivatives of area and perimeter are computed from calculating the derivatives of Eq. (3). After finding the α component of force contributions of three cells that vertex m is part of, we obtain the total force $f_{m,\alpha} = \sum_{i=1,2,3} f_{m,\alpha}^i$. In order to find the minimum energy configuration, we use FIRE (39). The minimization algorithm is stopped when $\max(\|\vec{f}_m\|)/N_v$, where N_v is the number of degrees of freedom (here the number of vertices), becomes less than 10^{-10} . During energy minimization, the network topology is updated using T1 transitions with an edge threshold of 10^{-5} .

Minimizing energy with respect to both physical and adaptive degrees of freedom

The internal degrees of freedom like $\{k_{p,i}\}$ and $\{p_{0,i}\}$ can be added in the minimization procedure to study the effects of these additional DOF on the mechanics of tissue. We study the effect of these different types of adaptive DOF one at a time. For example, when adding target shape factors $\{p_{0,i}\}$, we set $k_{a,i} = a_{0,i} = k_{p,i} = 1$ for all cells. We initialize $p_{0,i}$ values from a Gaussian distribution with a standard deviation of σ and mean $\langle p_{0,i} \rangle$. These $\{p_{0,i}\}$ are basically added in the minimization procedure similar to the physical DOF. The forces on these new DOF are computed as

$$f_{p_{0,i}} = -\frac{\partial e_i}{\partial p_{0,i}} = 2k_{p,i}(p_i - p_{0,i}). \quad (5)$$

The energy in Eq. (1) is then minimized with respect to both vertex positions (physical DOF) and these $\{p_{0,i}\}$ (adaptive DOF). We note that the convergence of the minimization algorithm

is more robust if we first minimize the physical DOF before including these additional DOF. In the case of $\{p_{0,i}\}$ DOF, if there are no constraints on the distribution of $\{p_{0,i}\}$, the system tunes these new DOF until $p_i - p_{0,i} = 0$, which results in a fluid state at the mean shape index of $\langle p_{0,i} \rangle \simeq 4.1$. In the case of $\{k_{p,i}\}$ DOF, without any constraints on the distribution of these new DOF, cells can arbitrary lower their $k_{p,i}$ during energy minimization.

To avoid these pathological states, we fix the distribution of adaptive DOF by constraining a set of moments, e.g., when adding $\{p_{0,i}\}$ as new DOF, we fix $\phi_k = \sum_i p_{0,i}^k$ where $k = \{m_1, m_2, \dots, m_n\}$, m_i is an integer value. With a sufficient number of moments, we find that the $\{p_{0,i}\}$ distribution is preserved during our energy minimization within an error margin. In presence of these constraints, the forces $f_{p_{0,i}}$ are modified in the constrained space of these moments. After finding the constraint Jacobian \mathbf{J} of these moments as

$$\mathbf{J}_{k,i} = \frac{\partial \phi_k}{\partial p_{0,i}} = k p_{0,i}^{k-1}. \quad (6)$$

The orthonormalized constraint basis \mathbf{J}_o can be computed using the Gram–Schmidt process. Therefore, the forces on $p_{0,i}$ in Eq. (5) are projected in this constrained space (30)

$$f_{p_{0,i}}^c = f_{p_{0,i}} - \mathbf{J}_o \mathbf{J}_o^T f_{p_{0,i}} \quad (7)$$

By using these constrained forces $f_{p_{0,i}}^c$, we ensure that the system does not alter the moments ϕ_k . Above, we explained the simulation procedure for adding $\{p_{0,i}\}$ as adaptive DOF. Adding other types of adaptive DOF like $\{k_{p,i}\}$ is done in a similar way. We observe that when constrained minimization is applied to adaptive degrees of freedom, there is a possibility that the system may not maintain the distribution within our desired error margin, particularly near the transition point. This happens even though all specified moments are preserved. To overcome this limitation, we have also employed a zero-temperature swap minimization technique. This approach precisely maintains the distribution of the adaptive degrees of freedom. We describe this minimization method in the subsequent section.

Zero-temperature swap minimization method

A useful limit of adding adaptive DOF is when the distribution of the adaptive DOF is exactly fixed. For instance, in the case of $p_{0,i}$ DOF, we start by drawing the target shape factors of cells from a Gaussian distribution with a standard deviation of σ and an average $\langle p_{0,i} \rangle$. To make sure that the distribution of $p_{0,i}$ is exactly fixed, we randomly swap $p_{0,i}$ of two cells, minimize the energy with respect to the vertex positions, and accept the swap move only if the energy decreases, illustrated by the following pseudocode:

$e_1 =$ Minimized energy wrt vertex positions

Swap cells i and j

$e_2 =$ Minimized energy wrt vertex positions

if $e_2 < e_1$ **then**

 Accept this swap move

else

 Reject this swap move

end if

The energy continuously decreases as a function of swap moves until it reaches a plateau. For system sizes studied, we find that typically $\sim 10^4$ swap moves results in a plateau.

Shear modulus calculation

As a measure for rigidity, we focus on the linear shear modulus G of the vertex model. It is important to note that while energy minimization might include adaptive degrees of freedom (DOF), these additional DOF are frozen during the calculation of G . Essentially, adaptive DOF are utilized solely to attain new configurations of the tissue. The solid-like state of the tissue is indicated by a shear modulus G greater than 10^{-4} , while a fluid-like state is characterized by G less than 10^{-4} . Notably, varying this small computational threshold does not change

our conclusions. The shear modulus is determined by computing the second derivative of the system's energy in relation to an infinitesimally small applied simple shear strain γ

$$G = \frac{1}{L^2} \frac{\partial^2 E}{\partial \gamma^2}, \quad (8)$$

where $L = \sqrt{N_c}$ is the lateral dimension of the simulation box. Rather than applying multiple strain deformations and numerically calculating this second derivative, the shear modulus can be efficiently determined from the Hessian matrix corresponding to the energy-minimized state (40). The elements of the Hessian are constituted by the second derivatives of the energy in relation to the positions of the vertices

$$D_{i\alpha, j\beta} = \frac{\partial^2 E}{\partial r_{i\alpha} \partial r_{j\beta}}, \quad (9)$$

where $r_{i\alpha}$ and $r_{j\beta}$ are the α component of the coordinates of vertex i and β component of the coordinates of vertex j , respectively. It can be shown that (40)

$$G = \frac{1}{L^2} \left(\frac{\partial^2 E}{\partial \gamma^2} - \sum_m \frac{1}{\omega_m^2} \left[\sum_{j,\alpha} \frac{\partial^2 E}{\partial \gamma \partial r_{j\alpha}} u_{j\alpha}^m \right]^2 \right), \quad (10)$$

where ω_m^2 are the non-zero eigenvalues of the Hessian matrix and $u_{j\alpha}^m$ are the corresponding normalized eigenvectors.

Acknowledgments

We thank Varda F. Hagh, R. Cameron Dennis, and Elizabeth Lawson-Keister for helpful discussions. MLM and SA were supported by Simons Foundation #454947, NSF-DMR-1951921 and SU's Orange Grid research computing cluster. IT was supported by the National Science Foundation through DMR-2005749 and AJL by the Simons Foundation #327939. AJL thanks CCB at the Flatiron Institute, a division of the Simons Foundation, and the Isaac Newton Institute for Mathematical Sciences at Cambridge University (EPSRC grant EP/R014601/1), for support and hospitality.

References

1. C. P. Goodrich, A. J. Liu, S. R. Nagel, *Physical Review Letters* **114**, 225501 (2015). Publisher: American Physical Society.
2. J. W. Rocks, *et al.*, *Proceedings of the National Academy of Sciences* **114**, 2520 (2017). Publisher: Proceedings of the National Academy of Sciences.
3. D. Hexner, A. J. Liu, S. R. Nagel, *Soft Matter* **14**, 312 (2018).
4. D. Hexner, A. J. Liu, S. R. Nagel, *Physical Review E* **97**, 063001 (2018).
5. J. W. Rocks, H. Ronellenfitsch, A. J. Liu, S. R. Nagel, E. Katifori, *Proceedings of the National Academy of Sciences* **116**, 2506 (2019). Publisher: Proceedings of the National Academy of Sciences.
6. N. Pashine, D. Hexner, A. J. Liu, S. R. Nagel, *Science Advances* **5**, eaax4215 (2019). Publisher: American Association for the Advancement of Science.
7. M. Stern, A. Murugan, *Annual Review of Condensed Matter Physics* **14**, 417 (2023).
_eprint: <https://doi.org/10.1146/annurev-conmatphys-040821-113439>.
8. D. Hexner, N. Pashine, A. J. Liu, S. R. Nagel, *Physical Review Research* **2**, 043231 (2020). Publisher: American Physical Society.
9. D. Hexner, A. J. Liu, S. R. Nagel, *Proceedings of the National Academy of Sciences* **117**, 31690 (2020). Publisher: Proceedings of the National Academy of Sciences.
10. B. Scellier, Y. Bengio, *Frontiers in Computational Neuroscience* **11** (2017).
11. M. Stern, D. Hexner, J. W. Rocks, A. J. Liu, *Physical Review X* **11**, 021045 (2021). Publisher: American Physical Society.

12. S. Dillavou, M. Stern, A. J. Liu, D. J. Durian, *Physical Review Applied* **18**, 014040 (2022).
Publisher: American Physical Society.
13. J. F. Wycoff, S. Dillavou, M. Stern, A. J. Liu, D. J. Durian, *The Journal of Chemical Physics* **156**, 144903 (2022).
14. S. Dillavou, *et al.*, Machine Learning Without a Processor: Emergent Learning in a Non-linear Electronic Metamaterial (2023). arXiv:2311.00537 [cond-mat].
15. A. Mongera, *et al.*, *Nature* **561**, 401 (2018).
16. X. Wang, *et al.*, *Proceedings of the National Academy of Sciences* **117**, 13541 (2020).
Publisher: National Academy of Sciences Section: Biological Sciences.
17. N. H. Claussen, F. Brauns, B. I. Shraiman, A Geometric Tension Dynamics Model of Epithelial Convergent Extension (2023). arXiv:2311.16384 [cond-mat, physics:physics, q-bio].
18. G. Erdemci-Tandogan, M. J. Clark, J. D. Amack, M. L. Manning, *Biophysical Journal* **115**, 2259 (2018).
19. P. C. Sanematsu, *et al.*, *Cells & Development* **168**, 203718 (2021).
20. L. Hufnagel, A. A. Teleman, H. Rouault, S. M. Cohen, B. I. Shraiman, *Proceedings of the National Academy of Sciences* **104**, 3835 (2007). Publisher: Proceedings of the National Academy of Sciences.
21. R. Farhadifar, J.-C. Röper, B. Aigouy, S. Eaton, F. Jülicher, *Current Biology* **17**, 2095 (2007).

22. J.-A. Park, *et al.*, *Nature Materials* **14**, 1040 (2015). Number: 10 Publisher: Nature Publishing Group.
23. D. Bi, J. H. Lopez, J. M. Schwarz, M. L. Manning, *Nature Physics* **11**, 1074 (2015). Number: 12 Publisher: Nature Publishing Group.
24. D. Bi, X. Yang, M. C. Marchetti, M. L. Manning, *Physical Review X* **6**, 021011 (2016). Publisher: American Physical Society.
25. M. Chiang, D. Marenduzzo, *Europhysics Letters* **116**, 28009 (2016). Publisher: EDP Sciences, IOP Publishing and Società Italiana di Fisica.
26. J. Devany, D. M. Sussman, T. Yamamoto, M. L. Manning, M. L. Gardel, *Proceedings of the National Academy of Sciences* **118**, e1917853118 (2021).
27. P. Sahu, *et al.*, *Soft Matter* **16**, 3325 (2020). Publisher: Royal Society of Chemistry.
28. X. Wang, C. M. Cupo, S. Ostvar, A. D. Countryman, K. E. Kasza, E-cadherin tunes tissue mechanical behavior before and during morphogenetic tissue flows (2024). Pages: 2024.05.07.592778 Section: New Results.
29. I. Tah, *et al.*, Minimal vertex model explains how the amnioserosa avoids fluidization during *Drosophila* dorsal closure (2023). BioRxiv: Pages: 2023.12.20.572544 Section: New Results.
30. V. F. Hagh, S. R. Nagel, A. J. Liu, M. L. Manning, E. I. Corwin, *Proceedings of the National Academy of Sciences* **119**, e2117622119 (2022). Publisher: Proceedings of the National Academy of Sciences.
31. O. K. Damavandi, V. F. Hagh, C. D. Santangelo, M. L. Manning, *Physical Review E* **105**, 025003 (2022).

32. A. Sharma, *et al.*, *Nature Physics* **12**, 584 (2016).
33. J. L. Shivers, S. Arzash, A. Sharma, F. C. MacKintosh, *Physical Review Letters* **122**, 188003 (2019).
34. M. Merkel, K. Baumgarten, B. P. Tighe, M. L. Manning, *Proceedings of the National Academy of Sciences* **116**, 6560 (2019).
35. S. Arzash, J. L. Shivers, F. C. MacKintosh, *Soft Matter* **16**, 6784 (2020).
36. X. Li, A. Das, D. Bi, *Physical Review Letters* **123**, 058101 (2019).
37. H. Honda, *Journal of Theoretical Biology* **72**, 523 (1978).
38. D. M. Sussman, *Computer Physics Communications* **219**, 400 (2017).
39. E. Bitzek, P. Koskinen, F. Gähler, M. Moseler, P. Gumbsch, *Physical Review Letters* **97**, 170201 (2006).
40. M. Merkel, M. L. Manning, *New Journal of Physics* **20**, 022002 (2018).
41. H. Bhaumik, D. Hexner, Mechanical regularization (2023). arXiv:2308.05050 [cond-mat].
42. M. Stern, A. J. Liu, V. Balasubramanian, *Physical Review E* **109**, 024311 (2024). Publisher: American Physical Society.
43. J. A. Zallen, R. Zallen, *Journal of Physics: Condensed Matter* **16**, S5073 (2004).
44. X. Yang, *et al.*, *Proceedings of the National Academy of Sciences* **114**, 12663 (2017). Publisher: National Academy of Sciences Section: Physical Sciences.
45. E. Teomy, D. A. Kessler, H. Levine, *Physical Review E* **98**, 042418 (2018). Publisher: American Physical Society.

46. B. Pisanty. (private communication, 2023).
47. M. F. Staddon, K. E. Cavanaugh, E. M. Munro, M. L. Gardel, S. Banerjee, *Biophysical Journal* **117**, 1739 (2019).
48. N. Noll, M. Mani, I. Heemskerk, S. J. Streichan, B. I. Shraiman, *Nature Physics* **13**, 1221 (2017).
49. C. S. O'Hern, L. E. Silbert, A. J. Liu, S. R. Nagel, *Physical Review E* **68**, 011306 (2003).
Publisher: American Physical Society.
50. A. Zaccone, *Theory of Disordered Solids: From Atomistic Dynamics to Mechanical, Vibrational, and Thermal Properties*, vol. 1015 of *Lecture Notes in Physics* (Springer International Publishing, Cham, 2023).

**Supplementary Information – Rigidity of Epithelial Tissues
as a Double Optimization Problem**

Details of the model

In these coarse-grained vertex models, tissue monolayers are described as a network of polygonal cells and the physical degrees of freedom (DOF) are the vertices of these polygons. Cellular properties and interactions are encoded in an energy function

$$E = \sum_i^N [K_{A,i}(A_i - A_{0,i})^2 + K_{P,i}P_i^2 + \gamma_i P_i], \quad (\text{S1})$$

where A_i and $A_{0,i}$ are the current and preferred cell areas, P_i is the cell perimeter, γ_i is the interfacial tension, and $K_{A,i}$ $K_{P,i}$ are the area and perimeter stiffnesses, respectively. The first term in energy is due to monolayer's resistance to height fluctuations and cells incompressibility. The active contractility of actomyosin cortex is captured as a quadratic penalty in cell perimeters in the second term of Eq. (S1). The competition between cortical tension and cell-cell adhesion of contacting cells results in an interfacial tension γ_i that is included in the last term.

By adding a constant term $P_{0,i} = -\gamma_i/(2K_{P,i})$ —a preferred perimeter—to Eq. (S1), we obtain

$$E = \sum_i^N [K_{A,i}(A_i - A_{i0})^2 + K_{P,i}(P_i - P_{i0})^2]. \quad (\text{S2})$$

Using the energy scale $\langle K_{A,i} \rangle \langle A_{0,i} \rangle^2$ and the length scale $\sqrt{\langle A_{0,i} \rangle}$, we can non-dimensionalize this elastic energy as

$$e = \sum_i^N [k_{a,i}(a_i - a_{0,i})^2 + k_{p,i}(p_i - p_{0,i})^2]. \quad (\text{S3})$$

Zero-temperature swap minimization method

Figure S1 shows the energy versus number of these zero-temperature swap moves at different values of the average target shape factor. The energy continuously decreases as a function of swap moves until it reaches a plateau. For system sizes studied, we find that typically $\sim 10^4$

swap moves results in a plateau. In the animation, we also show how these swap moves lower the shear modulus of the tissue by inducing spatial correlations between target shape factors.

Behavior of shear modulus

To analyze the scaling behavior of G as it approaches the critical point p_0^* , we employ a bisection method to differentiate between the rigid and floppy states of the tissue. We start with an initial bracket $[p_0^S, p_0^F]$, where $p_0^S = 3.65$ represents the solid state and $p_0^F = 4.2$ represents the fluid state. Subsequently, we iteratively narrow this bracket by conducting minimizations at its midpoint $p_0 = \frac{p_0^S + p_0^F}{2}$. We note that we do not include the box shear degrees of freedom in our minimization procedure. The criterion for adjusting the bracket is based on the shear modulus. Specifically, if the system has a shear modulus below a pre-defined threshold (in this case, 10^{-4}), the fluid boundary p_0^F is updated to the current midpoint p_0 . Conversely, if the shear modulus exceeds this threshold, the solid boundary p_0^S is updated in a similar manner. We perform at least 20 iterations of this bisection process to accurately locate the tissue's rigidity transition point.

Figure S2 illustrates the behavior of G versus its distance from the critical point for various system sizes. Notably, as we approach p_0^* , G exhibits a plateau that disappears in the thermodynamic limit. This observation aligns with previous work, indicating that such a plateau is absent in the shear-stabilized tissues (34).

Incorporating additional learning degrees of freedom leads to a decrease in tissue rigidity. Notably, introducing either $p_{0,i}$ or $a_{0,i}$ degrees of freedom leads to a more significant decrease in the shear modulus G compared to the effect of cell stiffness DOF. This is clearly shown in Figure S3. Interestingly, the scaling exponent of the shear modulus near the critical point remains unaffected as various learning DOFs are introduced, as demonstrated in Figure S4.

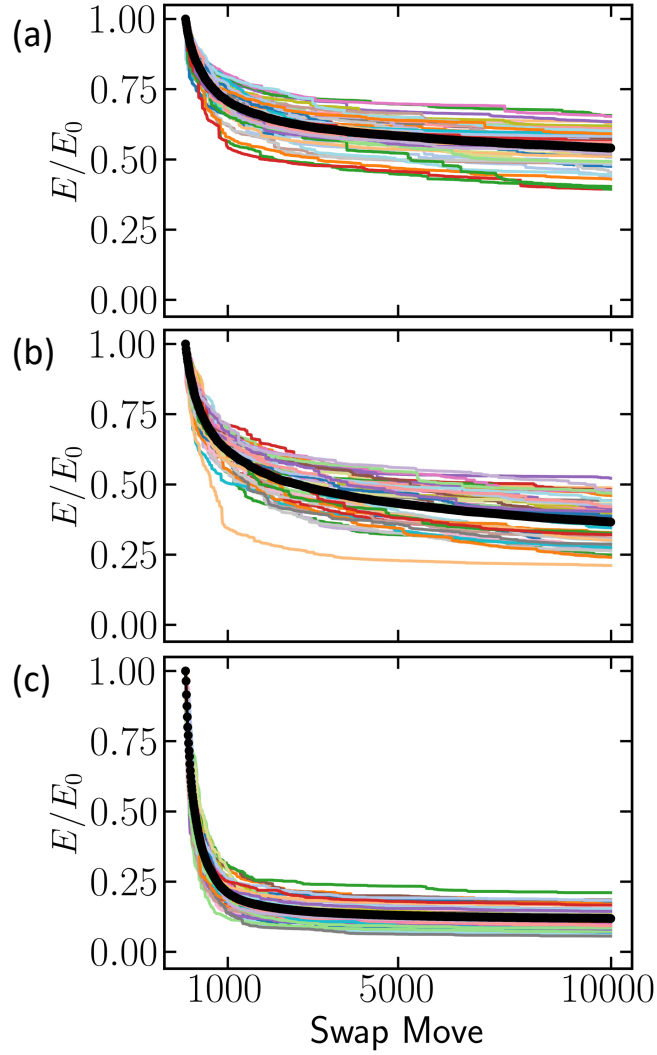


Figure S1: Energy ratio versus zero-temperature swap moves when the target shape factors of cells $\{p_{0,i}\}$ are drawn from a normal distribution with a standard deviation $\sigma = 0.2$. (a) For an average target shape factor of $\langle p_0 \rangle = 3.7$ (b) For an average target shape factor of $\langle p_0 \rangle = 3.75$ (c) For an average target shape factor of $\langle p_0 \rangle = 3.9$. The dark markers show the mean value, and the thin lines show 50 different samples. We used $N = 300$ cells in our simulations.

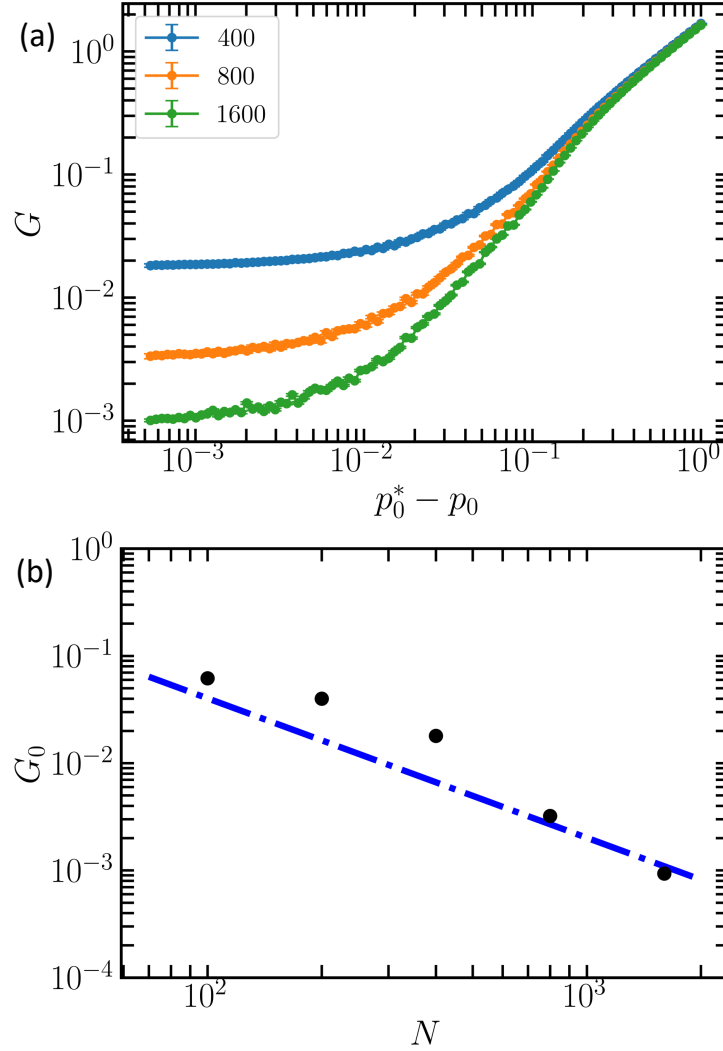


Figure S2: The behavior of shear modulus G versus the distance to the critical point without shear-stabilization. (a) The shear modulus G versus the distance to the rigidity transition point that was obtained using bisections. (b) The onset of shear modulus G_0 at the critical point p_0^* , i.e., the plateau in (a), versus system size N . This plateau vanishes at large N (the dashed line shows a slope of -1.3). These results are for energy minimized states with respect to only physical degrees of freedom. All cells here have the same p_0 values, i.e., there is no polydispersity in the p_0 parameter.

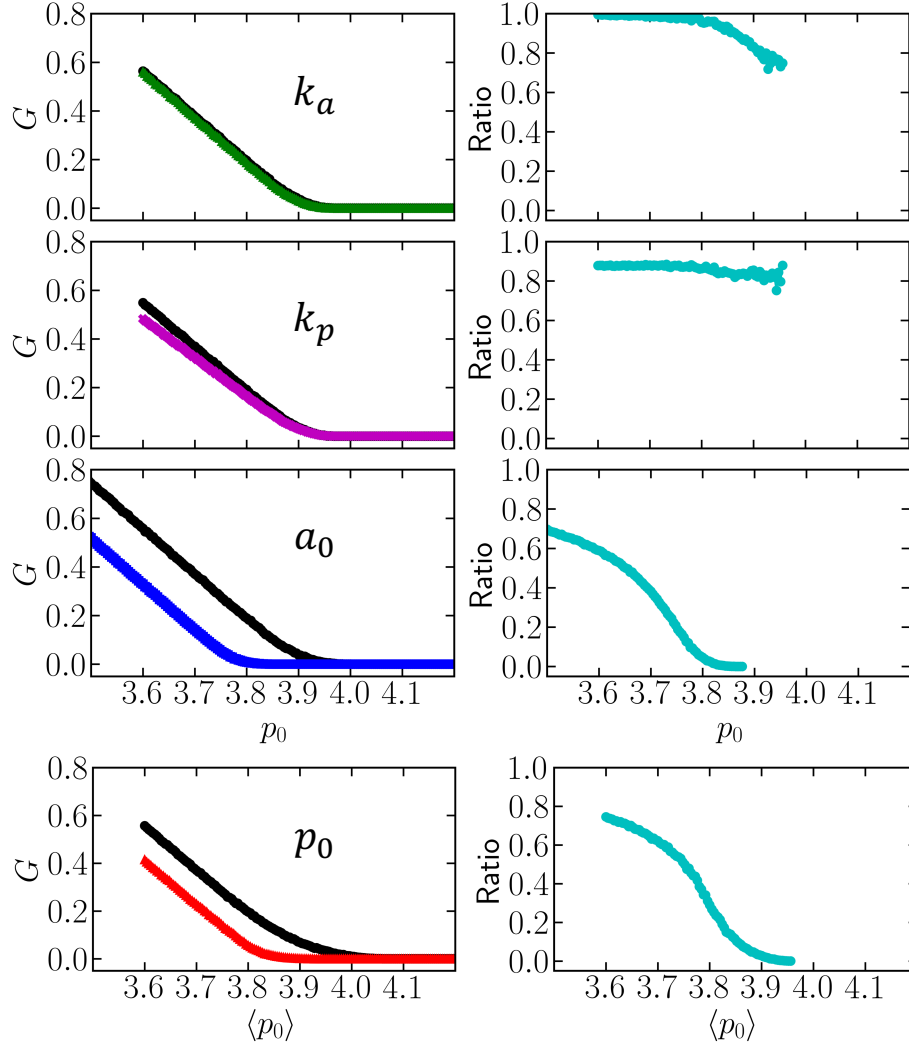


Figure S3: The effect of adding various learning DOF in vertex models on the shear modulus G . Each plot specifies the type of newly added DOF. Dark markers indicate the behavior of G in the absence of any learning DOF. For these simulations, the standard deviation for the distributions of learning DOF is fixed at $\sigma = 0.2$. On the right side of each plot, we display the ratio of G values obtained with the inclusion of new DOF compared to those without.

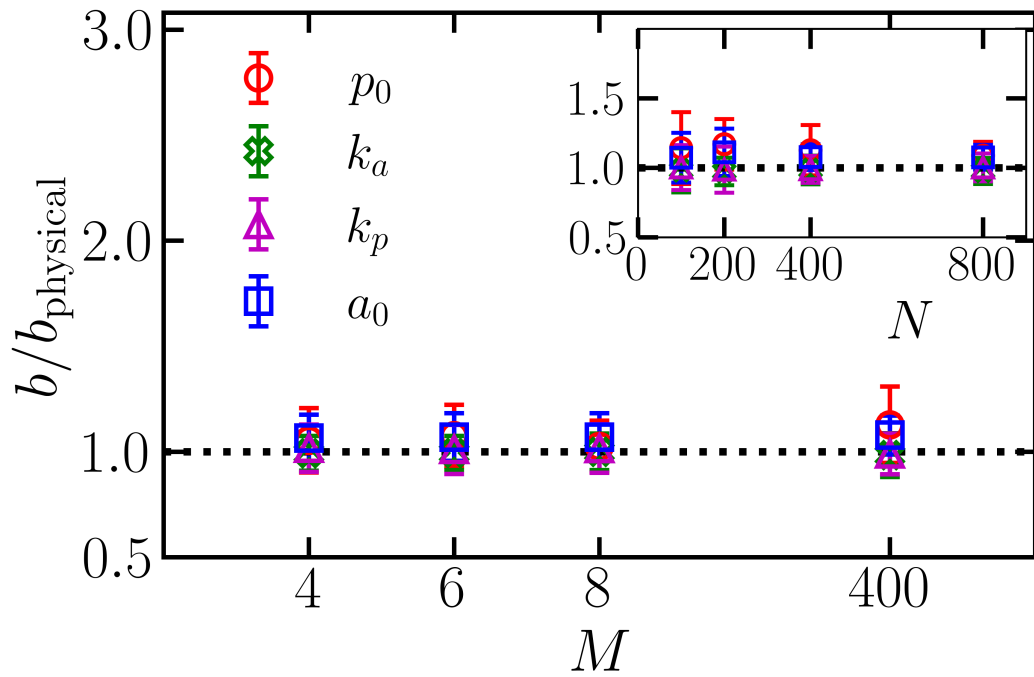


Figure S4: The effect of adaptive degrees of freedom on the scaling exponent b of the shear modulus as a function of number of constraints on the distribution. The zero-temperature swap system is indicated by 400 constraints, the number of cells in the tissue. The results are for a standard deviation of $\sigma = 0.2$ of adaptive degrees of freedom.

The effect of target area A_0

Yang et al. (44) have demonstrated that the manipulation of A_0 within a homogeneous system exhibits no impact on the mechanics of vertex models such as shear modulus and rigidity transition point. Here, we show that even in a heterogeneous system with polydispersity in A_0 , changing the average of A_0 distribution does not change the shear modulus behavior. Here, we assume that K_A , K_P , and P_0 are fixed and uniform for every cell.

$$\begin{aligned}
 E &= \sum_i K_A (A_i - A_{0i})^2 + K_P (P_i - P_0)^2 \\
 &= \sum_i K_A A_i^2 - 2K_A \sum_i A_i A_{0i} + \sum_i K_A A_{0i}^2 \\
 &\quad + \sum_i K_P (P_i - P_0)^2
 \end{aligned} \tag{S4}$$

We can find the following by adding and subtracting the term $\frac{K_A}{N} A_t^2$ to the equation above, where $A_t = \sum_i A_i = L^2$ represents the total tissue area

$$\begin{aligned}
 E &= \sum_i (A_i - \langle A \rangle)^2 + \frac{K_A}{N} A_t^2 - 2K_A \sum_i A_i A_{0i} \\
 &\quad + \sum_i K_A A_{0i}^2 + \sum_i K_P (P_i - P_0)^2
 \end{aligned} \tag{S5}$$

where $\langle A \rangle$ is the average area per cell, $\langle A \rangle = L^2/N$. Note that the terms $\frac{K_A}{N} A_t^2$ and $\sum_i K_A A_{0i}^2$ are constant offsets in the energy function. However, the term $2K_A \sum_i A_i A_{0i}$ can affect the forces on vertices. This term can be simplified by substituting $A_i = \langle A \rangle + \delta A_i$ and $A_{0i} = \langle A_0 \rangle + \delta A_{0i}$

$$\sum_i A_i A_{0i} = A_t \langle A_0 \rangle + \sum_i \delta A_i \delta A_{0i} \tag{S6}$$

The first term in the equation above indicates that the average value of the A_{0i} distribution affects the overall pressure of the system by a factor of $2K_A \langle A_0 \rangle$. This effect is similar to that of a system where all cells have homogeneous A_{0i} values. The second term in the equation can

cause the forces on vertices to change. This happens because there may be fluctuations in both the target area and the current area of the cell. We note that $\sum_i \delta A_i \delta A_{0i} = (N-1) \text{Cov}(A, A_0)$. By analyzing our simulation data, we find that this term is negligible compared to other terms in the elastic energy. As a result, even in the context of a heterogeneous tissue with a polydisperse distribution in A_{0i} , variations in the target area A_0 exert no significant impact on the shear modulus. Consequently, when A_{0i} values are introduced as learning degrees of freedom in tissues, changing their average $\langle A_{0i} \rangle$, while maintaining constant and uniform target perimeters $P_{0,i}$, does not result in any alteration of the shear modulus behavior.

Importantly, changing the width σ_{a_0} of the $A_{0,i}$ distribution in systems *without learning DOF* also does not have an impact on the transition point, in contrast to the behavior observed when changing the width of the p_0 distribution. The transition point is illustrated by the black data in Fig. S5 and main text Fig. 3(b). In other words, due to the arguments above, both non-dimensionalizations give the same results up to an arbitrary energy constant. However, because in heterogeneous systems the individual $\sqrt{A_{0i}}$ values can affect tensions, there is the possibility that changing the width of the area distribution could affect the rigidity transition point. As shown in Fig. S5, if one defines a dimensionless target shape index $\tilde{p}_{0,i} = P_{0,i}/\sqrt{\langle A_i \rangle}$, the rigidity transition shifts to lower values as a function of the width σ_{a_0} (green data). But, if one uses the dimensionless target shape index $p_{0,i} = P_{0,i}/\sqrt{A_{0,i}}$, as we have done throughout the manuscript, then the rigidity transition point is constant in those units (black data). This implies that the enhanced rigidity, as elucidated in Ref. (36), results from the heterogeneity in target shape indices ($p_{0,i} = P_{0,i}/\sqrt{A_{0,i}}$), rather than stemming from variations in $P_{0,i}$.

Details of tension percolation analysis

The rigidity transition in vertex models is governed by edge tensions. When the system is in the solid regime, the geometric incompatibility between the current and target cell perimeters leads

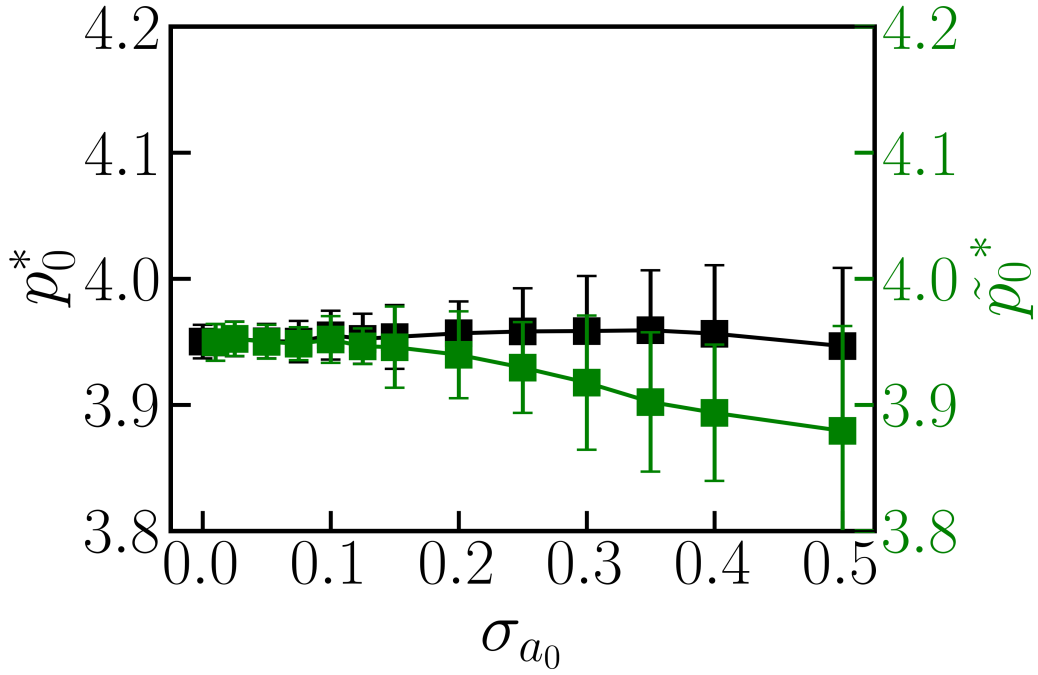


Figure S5: Comparison of rigidity transition points using two definitions of the target shape factor. The energy minimization is performed solely with respect to physical degrees of freedom with a distribution of a_{0i} values at different standard deviations σ_{a_0} . Here, we define $a_{0,i}$ as $A_{0,i}/\langle A_{0,i} \rangle$, with $\langle A_{0,i} \rangle = 1$. In the simulations, we maintain a fixed target shape factor defined as $p_{0,i} = p_0 = P_{0,i}/\sqrt{A_{0,i}}$. But we compute the target shape index in two different ways; in one case the shape index definition is based on the average cell area, denoted as $\tilde{p}_{0,i} = P_{0,i}/\sqrt{\langle A_i \rangle}$. In this case, $\langle A_i \rangle$ is set to 1, simplifying $\tilde{p}_{0,i}$ to $P_{0,i}$ (green data). In the other case we compute it based on the target areas of cells as in the main text, $p_{0,i} = P_{0,i}/\sqrt{A_{0,i}}$ (black data).

to the formation of a tensional cluster that spans the entire tissue. The mechanical stability of tissue is due to the presence of this percolated cluster. However, in the regime characterized by a large target shape factor, the tensional cluster fails to percolate, resulting in a fluid-like behavior of the tissue with a zero shear modulus. The transition point at which the tissue undergoes this rigidity change can be estimated using either tension percolation analysis or by examining the shear modulus.

To investigate tension percolation in our models, we begin by calculating the tensions, T_{ij} , on all edges ij between cells i and j

$$T_{ij} = 2K_{P,i}(P_i - P_{0,i}) + 2K_{P,j}(P_j - P_{0,j}). \quad (S7)$$

Edges with tensions below a certain threshold, set here at 10^{-6} , are considered to have zero tension (varying this small threshold has no significant effect on our results). We then identify the largest connected cluster of edges that have non-zero tensions. The system is classified as rigid if the linear size of this rigid tension cluster surpasses the dimensions of our simulation box. The linear size of this cluster is determined by $\max(\max(x_v) - \min(x_v), \max(y_v) - \min(y_v))$, where v denotes a vertex within this largest rigid cluster. By adjusting $\langle p_0 \rangle$ and examining the percolation of edge tensions, we are able to estimate the critical point of rigidity transition, denoted as p_0^* . To validate the tension-driven rigidity mechanism in our model, we compare the critical point derived from our percolation analysis with the results from shear modulus calculations, as shown in Fig. 1b. This agreement reinforces the idea that edge tensions are pivotal in governing the rigidity transition in the model, both when learning degrees of freedom are absent and present.

The effect of the width of p_0 distribution on shear modulus G

The shear modulus G in vertex models depends not only on the average target shape factor $\langle p_{0,i} \rangle$ but also on its polydispersity. Li et al., 2019 (36), demonstrated that when tissues are minimized

with respect to only physical degrees of freedom (i.e., vertex positions), the rigidity transition point increases with the standard deviation of the $\{p_{0,i}\}$ distribution. As we explore in the main text, incorporating $\{p_{0,i}\}$ as additional degrees of freedom in our energy minimization shifts the rigidity transition to lower values, regardless of the standard deviation of these degrees of freedom. Figure S6 shows how G varies with the average target shape factors, which are sampled from a normal distribution with different standard deviations σ (as specified in the legend).

Comparing the initial and final distributions

Incorporating new degrees of freedom into our tissue models necessitates careful management of their distributions to avoid trivial or unphysical outcomes post energy minimization. For example, adding cell stiffness parameters $\{k_{p,i}\}$ as degrees of freedom without any constraints on their distribution can result in tissues unrealistically driving these parameters to negative values. To mitigate this, our minimization process includes constraints on the distribution of these new degrees of freedom. This is achieved by fixing a certain number of distribution moments, as explained in the sections above. It is important to note, though, that deviations between the initial and final distributions are inevitable following our constrained minimization approach. These deviations tend to increase with fewer constrained moments. Figure S7 compares the initially set and the resultant distributions after applying constraints on six moments, specifically $\{-3, -2, -1, 1, 2, 3\}$. To ensure that possible variations in distributions do not impact our findings, we employed a zero-temperature swap minimization method (as explained in the above sections, as well). This technique precisely maintains the distribution fixed during energy minimization, relying solely on cell shuffling to achieve the lowest energy configuration.

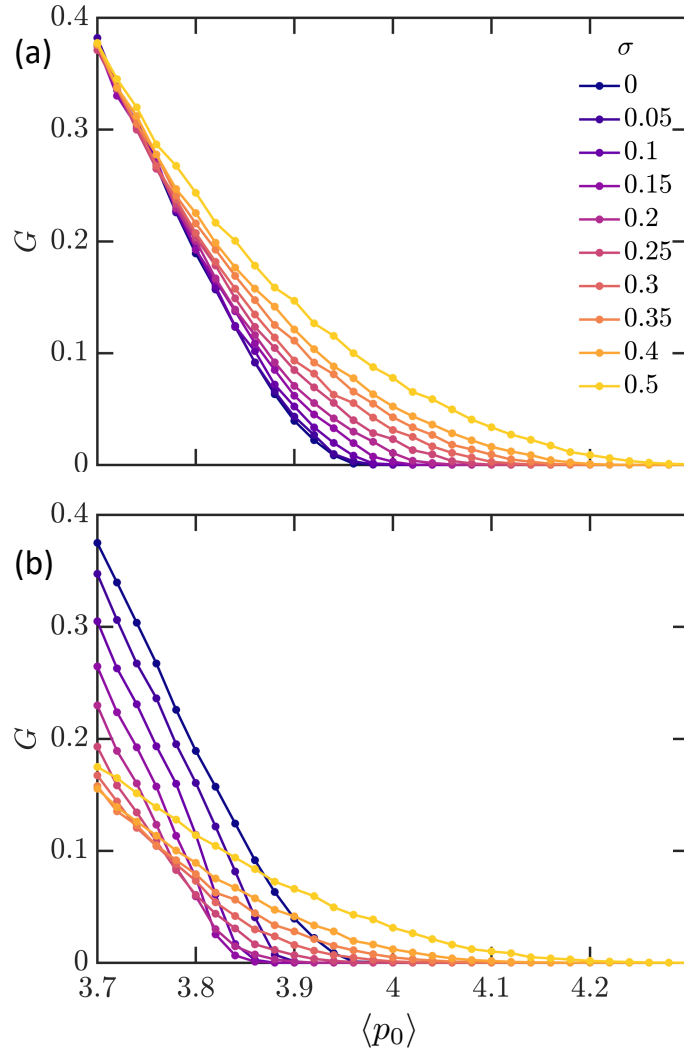


Figure S6: The effect of standard deviation of $p_{0,i}$ distribution σ on shear modulus G . (a) Shear modulus versus the average target shape factor for various values of the standard deviation as shown in the legend. These results are for tissues that are energy-minimized with respect to only physical degrees of freedom, i.e., vertex positions. (b) Same as (a) but in presence of learning degrees of freedom $\{p_{0,i}\}$ using zero temperature swap method.

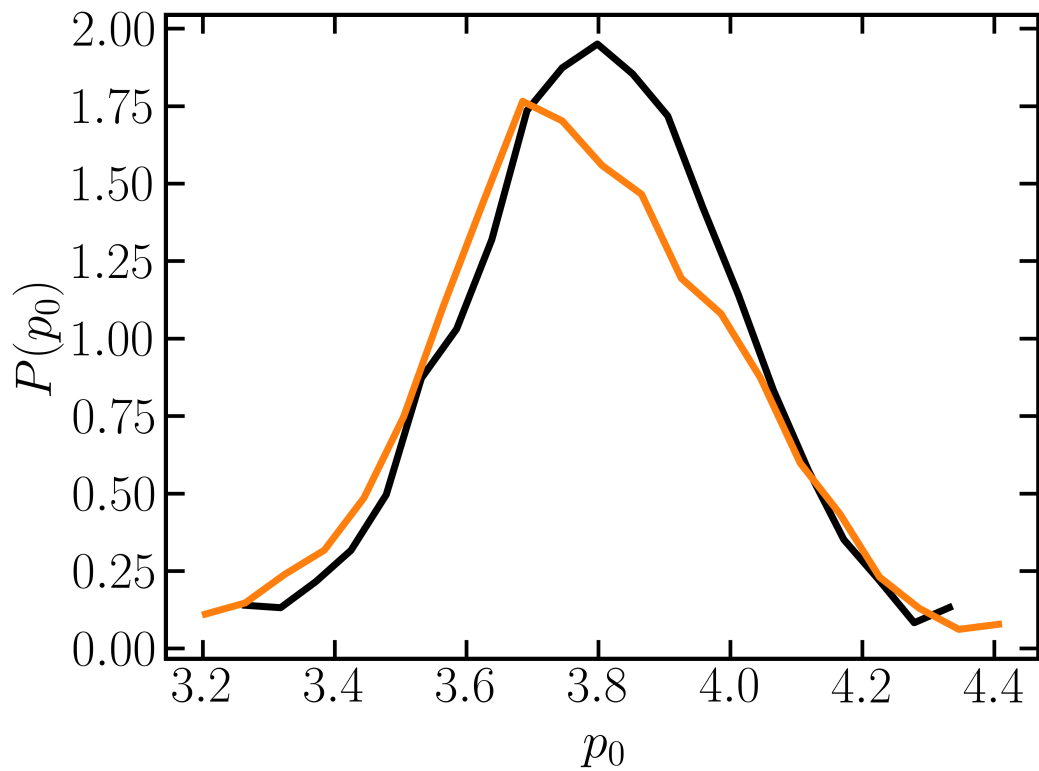


Figure S7: Distributions of target shape factors $\{p_{0,i}\}$ before (black) and after (orange) constrained minimization with $\langle p_0 \rangle = 3.8$ and $\sigma = 0.2$. Here, we fixed 6 different moments of the distribution during our minimization.

Correlations

To decipher the observed nonmonotonic variation in the rigidity transition point relative to the standard deviation σ of the p_0 or a_0 distributions, we investigated the correlations between p_i and $p_{0,i}$, as well as between a_i and $a_{0,i}$. These correlations were analyzed both when p_0 or a_0 were and were not included as new degrees of freedom. To measure these correlations, we employed Pearson's correlation coefficient, symbolized as ρ . Pearson's correlation coefficient quantifies the relationship between two data sets and is calculated by

$$\rho(x, y) = \frac{\sum (x_i - \bar{x})(y_i - \bar{y})}{\sqrt{\sum (x_i - \bar{x})^2 \sum (y_i - \bar{y})^2}}, \quad (\text{S8})$$

where x_i and y_i represent individual data points, while \bar{x} and \bar{y} denote their respective average values. Figure S8 exhibits the correlation patterns for different σ values. Notably, for higher $\sigma \gtrsim 0.15$, a strong correlation exists between p_i and $p_{0,i}$, even without considering $p_{0,i}$ as new degrees of freedom. Consequently, introducing these new DOF has minimal impact on exploring the tissue's energy landscape. This leads to a less pronounced shift in the rigidity transition point as the permitted fluctuations in $p_{0,i}$ increase a threshold $\sigma \approx 0.15$. A similar trend is observed when target areas $a_{0,i}$ are introduced as new DOFs, while maintaining a uniform target shape factor $p_{0,i} = p_0$ (refer to Fig. S8c and d).

Vibrational density of states

The vibrational density of states (VDOS) quantifies how vibrational modes are distributed across different frequencies in a system. To compute VDOS, first, the eigenvalue spectrum of the system's Hessian matrix λ_i are calculated at an energy minimum configuration. Eigenvalues close to zero, below 10^{-8} , are considered as zero modes and excluded from the VDOS analysis. The vibrational modes are computed as $\omega_i = \sqrt{\lambda_i}$, sorted and divided into bins. A normalized histogram is then generated to represent VDOS.

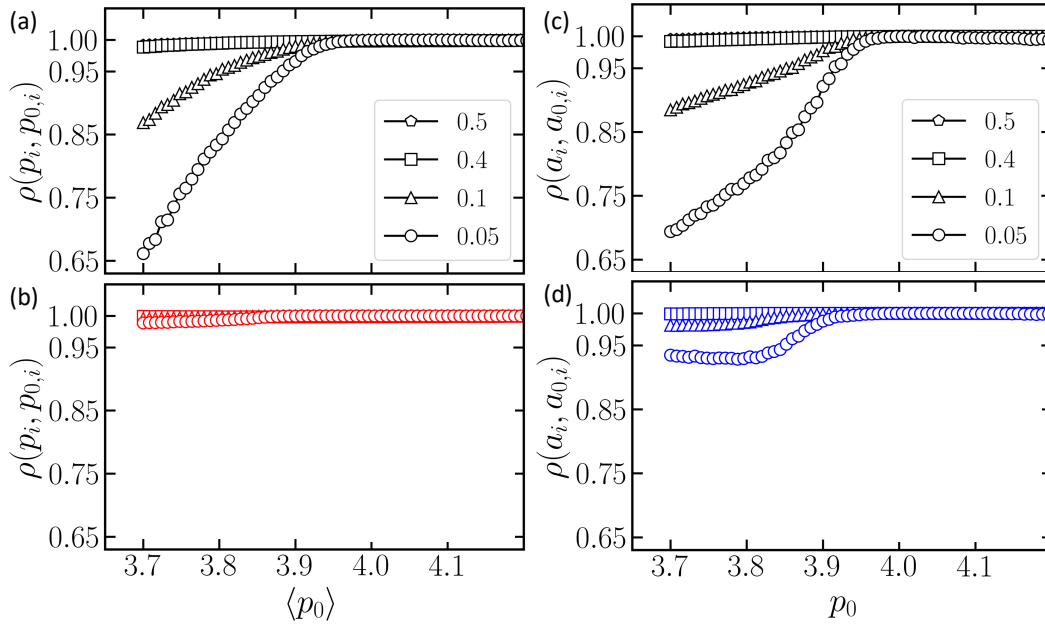


Figure S8: The behavior of Pearson's correlation coefficient. (a) $\rho(p_i, p_{0,i})$ versus the average target shape factor for different values of the standard deviation of the p_0 distribution as shown in the legend. Here, the system's energy is minimized only with respect to the physical degrees of freedom, i.e., vertex positions. (b) Same as (a) but the target shape factors $p_{0,i}$ are added as new DOF in the energy minimization. (c) Showing the correlations of target areas $a_{0,i}$ and current cell areas a_i in tissues without adding target areas as DOF and at uniform target shape factors $p_{0,i} = p_0$. (d) Same as (c) but $a_{0,i}$ are added as new DOF in the minimization process.

The vibrational density of states (VDOS) significantly affect the elastic properties of solids, both crystalline and disordered, and understanding its behavior under various conditions is crucial (49, 50). Thus we examine how VDOS responds to including different degrees of freedom (DOF) in tissues. Notably, VDOS conforms to Debye’s law, scaling as ω^{d-1} in the low-frequency limit, where d denotes the system’s dimensionality, both with and without these new DOF (Fig. S9).

Introducing the target shape factors $\{p_{0,i}\}$ or areas $\{a_{0,i}\}$ as adaptive degrees of freedom lead to a noticeable shift in VDOS towards lower frequencies, indicating a transition towards a softer solid state. However, adding stiffnesses as new DOF does not alter the overall behavior of the VDOS, only resulting in a slightly higher VDOS at the same p_0 values. This observation underscores that merely adjusting the stiffness within these systems does not fundamentally change their elasticity. On the other hand, introducing $\{p_{0,i}\}$ or $\{a_{0,i}\}$ as new DOF has a profound impact, pushing the VDOS of tissues to significantly lower frequencies compared to configurations without these additional DOF at similar p_0 (Fig. S9). This pronounced shift suggests that the presence of these new DOF facilitates the fluidization of tissues at a lower critical p_0 , highlighting a distinct softening effect. Such behavior vividly demonstrates how different types of DOF can influence tissue properties, suggesting why altering stiffness distributions alone cannot shift the rigidity transition in tissues. These VDOS findings align with our tension percolation analysis presented in the main text. Figure S10 shows the comparison of VDOS without and with adding target shapes ad DOF for a range of average target shapes. The intensified low frequency modes are clearly observed in this figure when $\{p_{0,i}\}$ are added as learning DOF.

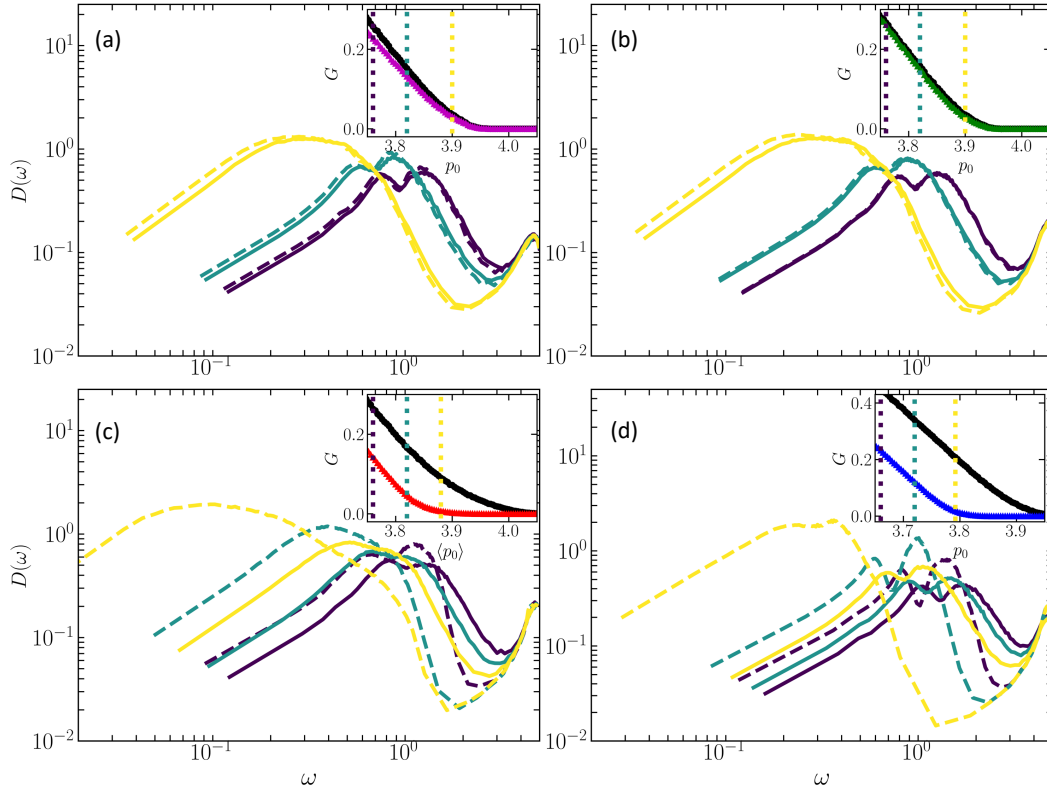


Figure S9: Vibrational density of states (VDOS) in tissues. (a) Density of states $D(\omega)$ versus frequency ω for tissues at three different target shape factors p_0 specified by vertical lines in the inset. The solid curves represent the VDOS for tissues minimized without incorporating $\{k_{p,i}\}$ as adaptive degrees of freedom, while the dashed curves depict the VDOS after adding $\{k_{p,i}\}$ to achieve minimum energy configurations, subsequently freezing these degrees of freedom. Inset: the black circles (purple triangles) show shear modulus as a function of p_0 without (with) adding $\{k_{p,i}\}$ as DOF. Panels (b), (c), and (d) are similar analysis of VDOS but for incorporating $\{k_{a,i}\}$, $\{p_{0,i}\}$, and $\{a_{0,i}\}$ DOF. All graphs maintain a constant standard deviation of $\sigma = 0.2$ for the adaptive DOF under study. Results are averaged across 50 realizations with 800 cells each.

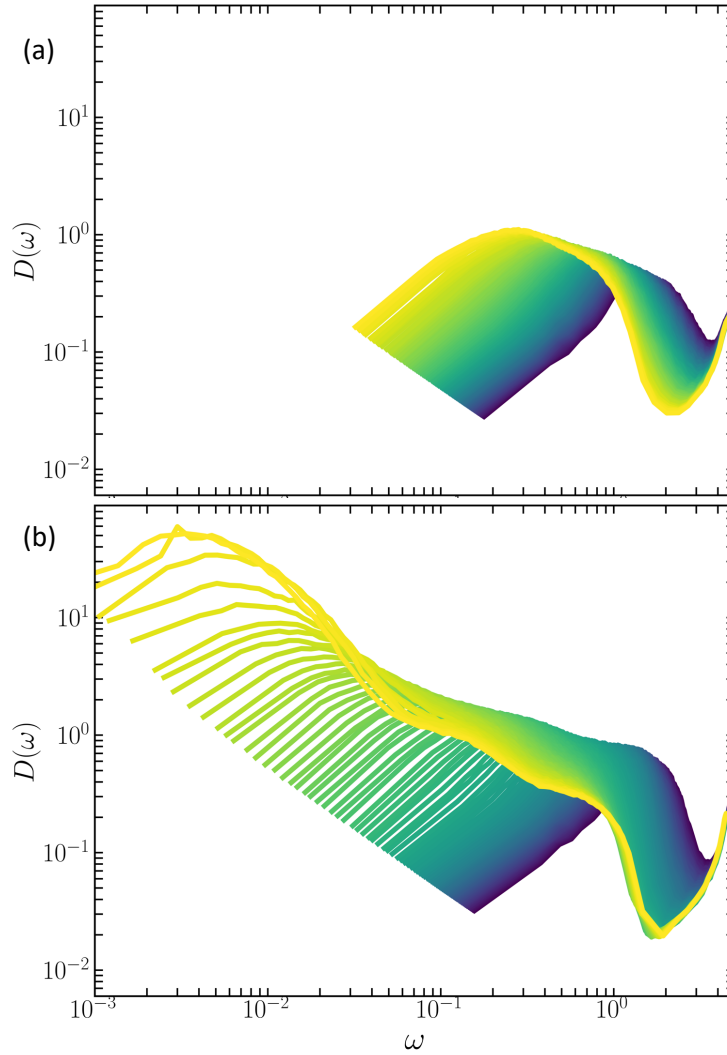


Figure S10: Vibrational density of states (VDOS) for average target shape factor $\langle p_0 \rangle$ ranging from 3.6 to 3.96, displayed in a gradient from dark to bright colors. (a) The tissue model is minimized without introducing new degrees of freedom (DOF). (b) The model is minimized with the inclusion of $\{p_{0,i}\}$ DOF. In both scenarios, the standard deviation of the p_0 distribution is fixed at 0.2. These results are based on averages from 50 simulations, each with 800 cells.

Structural features of tissues

To decipher the difference between microstructure of tissues with and without learning degrees of freedom, we study the structural features such as the pair correlation function $g(r)$ and the fraction of hexagonal cells. We compute $g(r)$ based on the cell centers that are calculated as center of masses of cell vertices in our vertex model. Figure S11 shows the behavior of $g(r)$ for systems with and without adding learning degrees of freedom $\{p_{0,i}\}$. In presence of $\{p_{0,i}\}$ DOF, tissues show sharper peaks in their pair correlation function depicting a more ordered structure. This effect becomes more pronounced near the transition point (Fig. S11).

To assess topological order in tissues, we examine the fraction of hexagonal cells, represented as f_6 . Figure S12 presents a heatmap of f_6 for tissues modeled with and without $\{p_{0,i}\}$ as degrees of freedom. Incorporating target shape factors as new DOF leads to an increased hexagonality, with f_6 potentially reaching up to 65%. The range of f_6 , from 0.3 to 0.65, is tunable through adjustments in the mean and standard deviation of the $\{p_{0,i}\}$ distribution, as shown in Figure S12b.

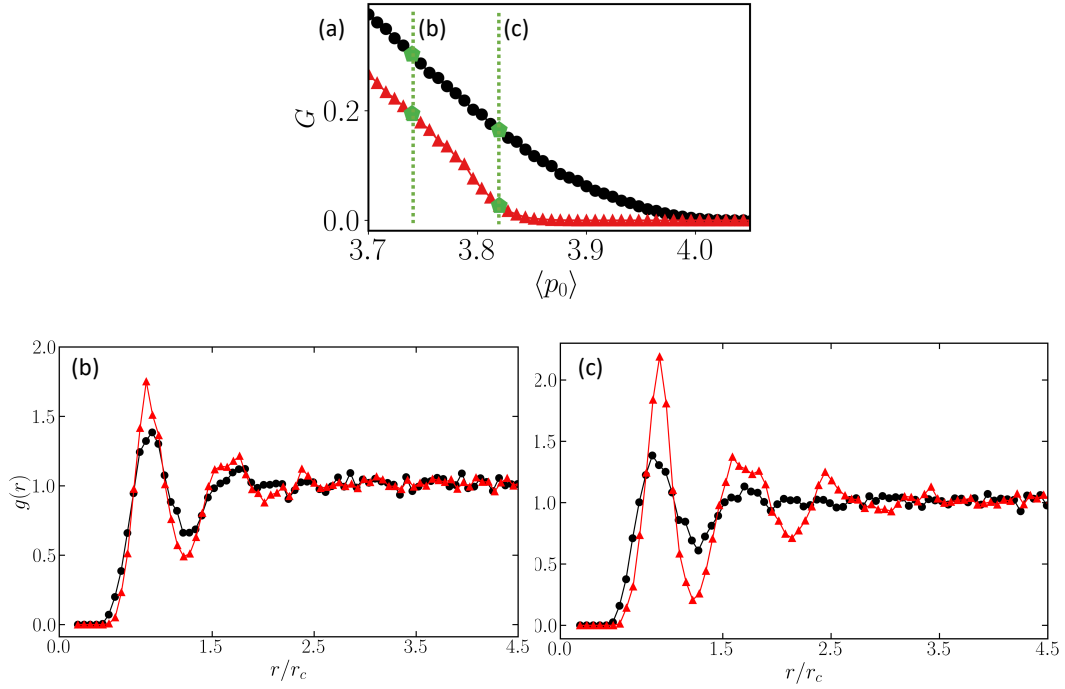


Figure S11: Comparison of pair correlation function $g(r)$ for tissues with and without adaptive degrees of freedom. (a) The linear shear modulus versus the average target shape factor with a standard deviation of $\sigma = 0.15$ of $\{p_{0,i}\}$ distribution. The black (red) data points correspond to minimized states without (with) including $\{p_{0,i}\}$ DOF. (b) $g(r)$ for the same average target shape factor $\langle p_0 \rangle$ (highlighted in the top plot of shear modulus). The dark circles (red triangles) correspond to tissues without (with) adding $\{p_{0,i}\}$ degrees of freedom. The x -axis is re-scaled with the typical half distance between cells. (c) Similar as (b) but for a higher value of $\langle p_0 \rangle$, as shown in the top plot. We used a system size of $N = 300$ cells.

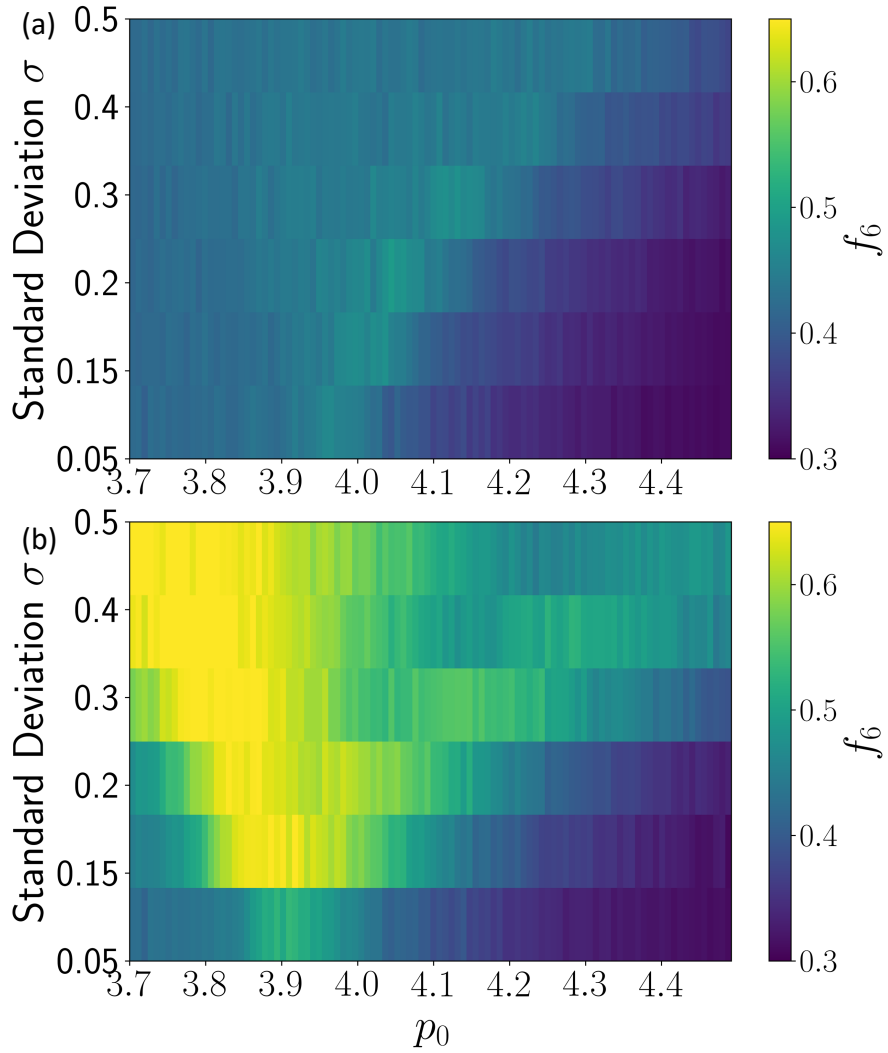


Figure S12: Comparison of hexagonal cell fractions f_6 for tissues with and without adding $\{p_{0,i}\}$ degrees of freedom. (a) Displays a heatmap of f_6 in tissues without introducing $\{p_{0,i}\}$ DOF, where the vertical axis represents the standard deviation and the horizontal axis the mean of the $\{p_{0,i}\}$ distribution; the color scale indicates f_6 values. (b) Shows the f_6 heatmap for tissues incorporating $\{p_{0,i}\}$ as adaptive DOF.